Dispersed phase back transport ultrafiltration of cutting oil emulsions with a spinning membrane disc geometry

Dal-Cin, Mauro; Lick, C. N.; Kumar, Ashwani; Lealess, S.

Publisher's version / Version de l'éditeur:
https://doi.org/10.1016/S0376-7388(97)00304-9
Journal of Membrane Science, 141, April 2, pp. 165-181, 1998

ELSEVIER

Journal of Membrane Science 141 (1998) 165–181

journal of MEMBRANE SCIENCE

Dispersed phase back transport during ultrafiltration of cutting oil emulsions with a spinning membrane disc geometry[1]

M.M. Dal-Cin*, C.N. Lick, A. Kumar, S. Lealess

National Research Council of Canada, Institute for Chemical Process and Environmental Technology, 1500 Montreal Rd., Ottawa, Ont., Canada K1A 0R6

Received 23 April 1997; received in revised form 10 November 1997; accepted 13 November 1997

Abstract

A commercial centrifugal rotary membrane module was used for the ultrafiltration of oil–water emulsions (droplet radius 50–3000 nm). This configuration can achieve high shear rates ($>10^5$ s^{-1}) which are decoupled from the bulk recirculation rate. Fluxes were in the pressure controlled regime above 600 rpm with transmembrane pressures up to 345 kPa. The pressure dependent flux behaviour suggests that concentration polarization or gel formation was minimal. The dominant back transport mechanism was determined by comparing various back transport mechanisms to the permeation drag force. Back transport mechanisms included Brownian diffusion, shear induced diffusion, lateral migration, viscous drag, centrifugal and DLVO forces. The effect of the membrane surface porosity and Sherwood's correction for Stokes's law on the permeation drag were also studied. Viscous drag was the dominant force on droplet sizes between 50–1000 nm and was the only mechanism which could overcome the permeation drag force. Lateral migration was significant for droplets between 1000–3000 nm which were present in small quantities. © 1998 Elsevier Science B.V.

Keywords: Ultrafiltration; Concentration polarization; Modules; Spinning disc

1. Introduction

Flux decline during various membrane processes can be the result of one, or more of the fouling mechanisms known as adsorption, pore plugging, concentration polarization or particle deposition. The relative importance of each of these mechanisms is determined by the interactions between the feed components, membrane material and morphology, and the operating conditions. Concentration polarization can be minimized by increasing the mass transfer coefficient or destabilizing the polarized layer at the membrane surface. A recent review of the many approaches studied is given in Ref. [1].

Of special interest are systems which decouple the shear rate at the membrane surface and the velocity of the bulk fluid. Mounting membranes on a rotating cylinder is one such approach which benefits from Taylor vortices and has been used as an analytical tool in membrane fouling studies [2,3]. Flootek (pre-

*Corresponding author. Fax: 613-941-2529; e-mail: mauro.dal-cin@nrc.ca

[1]Issued as NRCC No. 41962.

PII S0376-7388(97)00304-9

viously ABB Flakt CR) essentially uses a plate and frame module with a rotating blade to promote mixing at the membrane surface [4]. V-SEP (Vibratory Shear Enhancement Processes, New Logic International, CA, USA) uses a plate and frame geometry but achieves high shear rates at the membrane surface by vibrating the entire module in a two dimensional orbit in the plane of the membrane. Dynamic Microfiltration (Pall, USA) also uses modules with spinning discs over membranes to attain high shear rates. Spintek Centrifugal Membrane Filtration (CA, USA) produces modules with membranes mounted on spinning support discs, which also act as permeate carriers.

In this article we seek to determine the dominant back transport mechanism of emulsified oil droplets in water during ultrafiltration. A spinning membrane disc ultrafiltration module, ST-llL (Spintek) is used to generate high shear rates ($>10^5\ s^{-1}$). The application of the limiting flux models may not be appropriate to the present work as the assumption of gel or cake dominated flux was not met.

In lieu of this, a force balance approach was used to determine if an oil droplet would remain stationary on the membrane surface. Forces acting against permeation drag, F_P, include viscous drag due to the local shear rate, F_V, shear enhanced diffusion, F_S, Brownian diffusion, F_B, lateral migration, F_L, centrifugal forces, F_C, and electrostatic repulsion. These forces are normalized by the permeation drag force, F_P, using Sherwood's correction to Stokes's law [5]. The effect of surface porosity on the local permeation velocity is discussed and deemed to be insignificant in this work.

Viscous drag on a particle resting on a surface in a flow field [6] was the dominant force over the entire range of droplet sizes, with F_V/F_P greater than unity. Shear enhanced diffusion and lateral migration were not significant for the majority of the droplet radius range (50–3000 nm) under consideration. Lateral migration was significant only for droplet radii >1000 nm.

Possible sources of error in predicting oil droplet deposition can arise from estimates of the shear rate, the wide range of oil droplet sizes or Sherwood's correction factor (via the skin layer thickness).

2. Theory

2.1. Film theory

The permeation flux through a membrane can be described by a mass balance at the membrane surface [7]

$$J_v = \frac{D}{\delta}\ln\left(\frac{C_m - C_p}{C_b - C_p}\right) = k\ln\left(\frac{C_m - C_p}{C_b - C_p}\right) \approx k\ln\left(\frac{C_m}{C_b}\right) \tag{1}$$

where C_m, C_b, and C_p are the solute concentrations at the membrane surface, bulk and permeate, respectively. The solute diffusivity, thickness of the polarized layer and mass transfer co-efficient are denoted by D, δ and k, respectively. When dealing with oil–water emulsions the observed retention was generally greater than 96% and so $C_p \approx 0$. The total carbon (TC) concentration in the permeate was high, several hundred ppm, and was primarily excess surfactant.

The mass transfer co-efficient is related to the Sherwood, Reynolds and Schmidt numbers by

$$\mathrm{Sh} = \frac{kd_h}{D} = (\text{constant})\mathrm{Re}^{\alpha}\mathrm{Sc}^{b} \tag{2}$$

where d_h is the hydraulic diameter. The exponent of Re varies from 0.5 to 1 depending on the conditions and range of Re under consideration, but is generally close to 0.75 for turbulent flow and 0.33 for laminar flow.

The flow with a rotating disc geometry can be characterized by two Reynolds numbers [8]

$$\mathrm{Re}_s = \frac{\omega s^2}{\nu} \quad \text{and} \quad \mathrm{Re}_r = \frac{\omega r^2}{\nu} \tag{3}$$

where ω is the rotational velocity (rad/s), ν is the kinematic viscosity, s is the gap between the rotating disc and the adjacent, parallel surface and r is the local radius. Re_s compares the total liquid gap to the boundary layer thickness while Re_r characterizes the ratio of inertial to viscous forces. Using Eqs. (1)–(3), the flux dependence on the rotor speed should be

$$J_v = k\ln\left(\frac{C_m}{C_b}\right) \propto \omega^{\alpha}\ln\left(\frac{C_m}{C_b}\right) \tag{4}$$

The dominant back transport mechanism with low molecular weight solutes is Brownian diffusion, with the diffusion co-efficient estimated from

$$D_B = \frac{k_B T}{6\pi\mu r_p} \quad (5)$$

where k_B is the Boltzman constant and T the absolute temperature. When the Brownian diffusivity is used for ultrafiltration and microfiltration of large particles the film theory underpredicts the experimental flux by one or two orders of magnitude [9,10]. This discrepancy is attributed to the contribution of other back transport mechanisms which dominate at larger solute–particle sizes. The importance of these factors depends on the particle size and the transition from one dominant mechanism to another has been shown to result in a minimum [11,12]. These alternative mechanisms for back diffusion and their relevance to the current work are discussed below.

2.2. Forces acting on an oil droplet

2.2.1. Methodology

The significance of each back transport mechanism is determined by normalizing it with the permeation drag force, F_P. As an example, the force on a particle due to lateral migration, F_L, is expressed as F_L/F_P. A value less than unity should not be possible and so back transport must be by some alternative mechanism. The dominant back transport mechanism should have a force ratio greater than, or equal to, unity.

Force balances have also been used to evaluate particle trajectories to determine if they would remain entrained in the bulk fluid flow or deposit on the membrane surface [13–15]. Aubert et al. [16] showed that a critical shear stress, which can be related to a force on the deposited particles, was required before a preformed carbon cake was eroded during microfiltration with a spinning disc.

The various back transport mechanisms are typically described as diffusivity (shear enhanced or Brownian), velocity (lateral migration) or a force (viscous drag, permeation drag, centrifugal or DLVO). The forces acting on a particle on the surface of a spinning membrane disc are similar to conventional cross flow with the addition of centrifugal acceleration and radial shear components, Fig. 1.

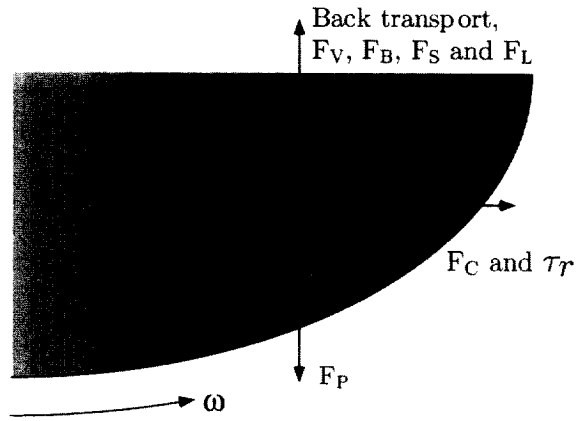

Fig. 1. Schematic representation of various forces acting on an oil droplet on a membrane disc spinning with angular velocity ω. Droplet transport to the membrane surface is due to permeation drag, F_P. Back transport is by Brownian diffusion in addition to radial and angular shear components, τ_r and τ_θ. Shear components result in viscous drag, F_V, shear enhanced diffusion, D_S, and lateral migration, D_L.

We shall restrict the force balance approach to the onset of mass transfer limited flux. This simplifies the analysis with respect to Sherwood's correction factor (Section 2.2.2) and limits particle–particle interactions and changing solution properties at the membrane surface. Surface roughness, due to the membrane or cake, can also play a role in determining the extent of droplet deposition. This case was presented by Lu and Ju [17] and used by Stamatakis and Tien [18]. We shall consider a smooth surface for our analysis.

The experimental variables and adjustable parameters are summarized in Table 1. The force ratios are the response for this system. The droplet size, viscosity and density, are arrived at by the nature and concentration of the oil and surfactants. Therefore they are not considered as controllable variables in this work.

2.2.2. Permeation drag force

Sherwood [5] derived the force on a particle being pulled away from a permeable surface. This force was essentially a corrected Stokes's force taking into account the permeability of the membrane and particle size. The correction factor reaches asymptotic solutions for large and small values of the dimensionless permeability $\beta = l/r_p^2$. In the absence of a cake, the

Table 1
Summary of experimental variables and adjustable parameters used in evaluation of forces due to permeation drag force and back transport mechanisms

Experimental variables	Adjustable parameters
τ via ω, rotor speed, 100–1800 rpm, (10.5–188.4 rad/s)	δ_m in Sherwood's correction factor, 1 μm (assumed)
P, operating pressure, 69–310 kPa	K, constant in τ correlations (0.9 assumed)
T, temperature, 25°C	
ϕ, droplet volume concentration	

permeability used by Sherwood, $l=\delta_m/R_m$, is that of the membrane where δ_m is the skin layer thickness (assumed to be 1×10^{-6} m). The permeation drag force is

$$F_P = 6\pi\mu r_p \upsilon \cdot 0.36\beta^{-2/5} \quad \beta < 0.01 \tag{6}$$

A second correction may be required for the effect of the membrane's surface porosity. The permeate velocity, υ, is typically determined by υ=flux/permeation area. However the permeate velocity in the vicinity of the pore will be somewhat higher [19,20] and is a function of the surface porosity ε

$$\upsilon = \frac{\text{volumetric flux}}{\text{permeation area} \cdot \varepsilon} \tag{7}$$

Corrections for the surface porosity were not used in this work and will be discussed in a later section.

2.2.3. Shear forces

The effects of viscous shear may be described by several methods, the viscous drag force on a particle in a shear field, shear enhanced diffusion or lateral migration. All of these cases will be considered and compared to the permeation drag force.

Stamatakis and Tien [18] used the expression derived by O'Neill [6] for the drag force exerted on a single particle on a rigid surface

$$F_V = 1.7009(6\pi\mu r_p \upsilon) = 1.7009(6\pi\mu r_p^2 \tau) \tag{8}$$

where τ is the shear rate at the wall and the fluid velocity, υ, is evaluated at the droplet midpoint assuming the velocity is a linear function of the distance from the membrane. This approach for estimating the velocity of the liquid around a droplet will be limited to the boundary layer. Estimation of the boundary layer will be discussed in Section 5.2.

The shear enhanced diffusivity, D_S, arises due to the interaction of particles as they undergo random displacements from flow streamlines in shear flow. Wiesner et al. [21] used the concentration corrected D_S of Leighton and Acrivos [22]

$$D_S = 0.3\tau \frac{\mu_o}{\mu_\phi} r_p^2 \phi^2 (1 + 0.5e^{8.8\phi}) \tag{9}$$

where ϕ is the volume fraction of the particles and μ_o/μ_ϕ is the ratio of the bulk and local viscosities. The viscosity correction is taken as unity in this case as concentration polarization is minimal.

Cohen and Probstein [23] used a characteristic Brownian velocity, $v_B=D_B/r_p$. We shall extend this approach to obtain a characteristic velocity for a droplet undergoing shear enhanced diffusion $v_S= D_S/r_p$. These velocities will be used with Stokes's law in order to evaluate Brownian and shear enhanced diffusion "forces".

Particles will also have a lateral migration or lift velocity, v_L, resulting from significant nonlinear interactions of particles with the flow field [1]. This mechanism has been studied extensively for several geometries and flow conditions, given the high Reynolds numbers in the system used in this work, albeit of very different geometry, the derivation of Drew [24] is used

$$v_L = \left(\frac{0.577}{16}\right)\frac{\tau^2 r_p^3}{\nu} \tag{10}$$

2.2.4. DLVO forces

Cutting oil–water emulsions are stabilized by electrostatic repulsion [25]. Oil droplet surfaces consist of the ionic portions of the surfactants and emulsifiers (primarily sodium oleate and potassium dodecyl sulfonate in this work). DLVO (Deryaguin, Landau, Verwey, Overbeek) theory can describe the summation

of electrostatic repulsion and attractive van der Waals forces of these mixtures. The case of equal size spheres approaching each other can be used to approximate the case of an oil droplet approaching the membrane surface which has similar properties after adsorption of surfactant. For small zeta potentials, ζ<30 mV [25]:

$$V_T = V_R + V_A = 2\pi r_p \epsilon \zeta^2 \exp\left(-\frac{h}{\lambda_D}\right) + \frac{r_p A}{12h} \quad (11)$$

The zeta potential, Debye length, λ_D, and separation distance, h, determine the magnitude of the force and the distance over which the repulsion–attraction are significant, the remaining constants are defined in the list of symbols. The Debye length can be estimated from λ_D=0.304$M^{-1/2}$ nm where M is the molar concentration of a symmetric electrolyte with a valence of unity.

Electrostatic repulsive forces were shown to control the flux during colloidal fouling of reverse osmosis membranes, Cohen and Probstein [23], and protein microfiltration, Palecek and Zydney [26]. McDonogh et al. [27] proposed a correction term for the conventional film model for charged colloids to explain the flux anomaly. The term accounting for DLVO forces could be significant, particularly with longer Debye lengths and particle sizes less than 100 nm. Bacchin et al. [28] developed a model in which a critical flux is based on the potential energy barrier between particles, V_B, diffusivity and the boundary layer thickness:

$$J_{crit} = \frac{D}{\delta} \ln\left(\frac{V_B}{\delta}\right) \quad (12)$$

where

$$V_B = \int_0^\infty (e^{V_T/kT} - 1)\, dx$$

and V_T is given by Eq. (11).

2.2.5. Centrifugal and buoyancy forces

The centrifugal force, F_C, can be determined from

$$F_C = ma = \frac{4}{3}\pi r_p^3 \rho_p \times \omega^2 R \quad (14)$$

where a is the centrifugal acceleration, m is the droplet mass, r_p is the droplet radius, ρ_p the droplet density, R is the radius of rotation and ω is the rotational velocity in rad/s. This approach assumes that the oil droplets behave as individual entities. The centrifugal force can be considerably greater if the droplets are self associating or a gel–cake forms.

The buoyancy force is based on the density difference of the droplet and bulk fluid,

$$F_{buoy} = \frac{4}{3}\pi r_p^3 (\rho_l - \rho_p) g \quad (15)$$

The density of the oil droplet is assumed equal to that of the bulk oil at 850 kg/m^3. The buoyancy force will be acting with and against the permeation drag on the bottom and top sides of the disc, respectively.

2.3. Shear rates

Estimates of the shear rate are required to determine the effective diffusion co-efficient, lateral migration velocity and viscous drag force exerted on a droplet on the membrane surface. The shear rates of spinning disc systems in a large space have been described by Aubert et al. [16] and Kozinsky and Lightfoot [29]. Spinning disc systems have been described by several authors [8,30,31]. Murkes and Carlsson [8] describe the shear stress for configurations with wide and narrow gaps more suited to this work.

The expressions for the shear stress are:

Region 1 $\tau_1 = \nu\omega r/s \quad Re_s < 4,\ Re_r < 2 \times 10^5$ (16)

Region 2 $\tau_2 = 1.81\rho\nu^{1/2}(K\omega)^{3/2} r \quad Re_s > 4,\ Re_r < 2 \times 10^5$ (17)

Region 3 $\tau_3 = 0.008\rho(\omega r)^{1.75}(\nu/s)^{0.25} \quad s/r < 0.05,\ Re_r > 2 \times 10^5$ (18)

Region 4 $\tau_4 = 0.057\rho\nu^{0.2}(K\omega)^{1.8} r^{1.6} \quad s/r > 0.05,\ Re_r > 2 \times 10^5$ (19)

The boundary layers for Regions 1 and 2 are laminar with merged and separate boundary layers, respectively. Regions 3 and 4 are turbulent, in the narrow gap case the boundary layers are merged and with a wide gap they are separate and distinct. A turbulent core of liquid will also exist in the latter case and rotate with a velocity $K\omega$. K is a co-efficient which has been experimentally determined as 0.4 to 0.5 for a

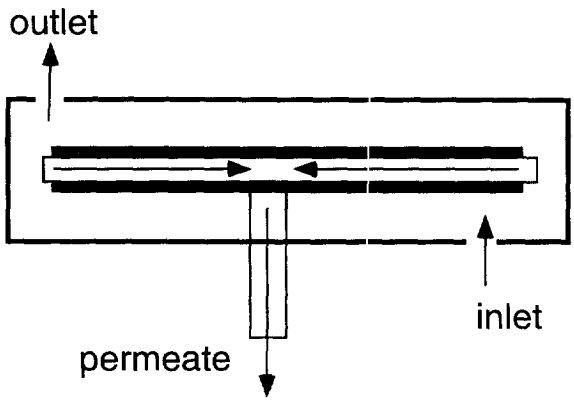

Fig. 2. Cross section of the ultrafiltration module. Note that membrane is sealed at the outer circumference of the the disk and permeate is collected at the shaft center.

smooth disc and 0.9 for rotating discs with 8 radial vanes.

The transition from region 4 to 2 occurs at ~225 rpm, but below this speed both correlations predict similar shear stresses. The ST-IIL borders on the wide–narrow gap criterion with s/r=0.069. The ratio of τ_4/τ_3 ranges from 5.6 to 6.2 between 225 and 1800 rpm. The τ_4 values are used to estimate the fluid velocity in the vicinity of the membrane surface in this work,

$$v = \tau_4 \times h \tag{20}$$

2.4. Pressure effects with a spinning disc

The ST-IIL uses a membrane mounted on a spinning disc with seals at the outer circumference. The permeate is collected through the rotor shaft via permeate carrier, Fig. 2. An operational consequence of this design is a negative pressure, P_{perm}, due to the centrifugal force of the permeate:

$$P_{\text{perm}} = \tfrac{1}{2}\rho\omega^2 r^2 \tag{21}$$

P_{perm} can be significant when using pilot or full scale systems operating at high rpm, reaching 151 kPa at 188.4 rad/s (1800 rpm). As will be seen in Section 5, it is useful to express the experimental flux as a function of the effective transmembrane pressure, P_{eff}, rather than the actual operating pressure, P_0. Analogous pressure corrections were used by Belfort et al. [2] to correct for the centrifugal pressure of the permeate in a rotating cylinder geometry. Consider the absolute flux across the disc, $J_{\text{v tot}}$:

$$J_{\text{v tot}} = \frac{P_{\text{eff}}A_{\text{tot}}}{\mu R_{\text{m}}} = \frac{1}{\mu R_{\text{m}}}\int_{r_i}^{r_o}(P_{\text{o}}(r) - P_{\text{perm}}(r))\mathrm{d}A \tag{22}$$

where $P_{\text{o}}(r)$ is constant. Eq. (22) can be integrated between the inner and outer edges of the disc, r_{i} and r_{o}, respectively:

$$\begin{aligned} P_{\text{eff}}A_{\text{tot}} &= \textstyle\int_{r_i}^{r_o} P_{\text{o}}(r)\mathrm{d}A - \int_{r_i}^{r_o} P_{\text{perm}}(r)\mathrm{d}A \\ P_{\text{eff}}\pi(r_{\text{o}}^2 - r_{\text{i}}^2) &= P_{\text{o}}\textstyle\int_{r_i}^{r_o} 2\pi r\mathrm{d}r - \int_{r_i}^{r_o}\left(\tfrac{1}{2}\rho\omega^2 r^2\right)2\pi r\mathrm{d}r \\ P_{\text{eff}} &= P_{\text{o}} - \tfrac{\rho\omega^2}{4}(r_{\text{o}}^2 + r_{\text{i}}^2) \end{aligned} \tag{23}$$

The permeate back pressure can be used to correct the operating pressure to obtain the average transmembrane pressure. The flux can be corrected for the permeate back pressure using:

$$J_{\text{vc}} = J_{\text{v}} \times \frac{P_{\text{o}}}{P_{\text{o}} - P_{\text{eff}}} \tag{24}$$

3. Materials

The membrane module is described as a centrifugal ultrafiltration unit, model ST-IIL. The total permeation area is 0.05 m^2, with two membrane sheets (0.203 m diameter) mounted on a PVC disc. A permeate carrier between the membrane sheets and disc carries the permeate to the bored out rotor shaft. A baffle plate with four vanes is mounted on each side of the spinning disc. The maximum rotor speed is 1800 rpm via a 2 HP continuously variable speed motor with a belt drive. Rotor speeds are set with an optical tachometer. Maximum operating pressure and temperature on this unit are 310 kPa and 50°C, other versions can operate at higher pressures and temperatures. A shut off switch and alarm are provided for low feed pressures and excessive vibration. The former guards against delaminating membranes due to the permeate backpressure while the latter protects the unit itself.

Cutting oil (Doall No. 407) emulsions were prepared at various concentrations in tap water which had been filtered with a 0.2 cartridge filter. The viscosity of

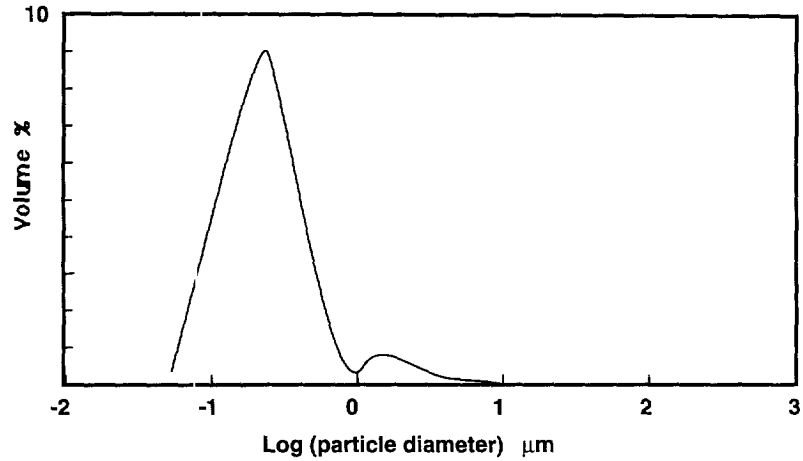

Fig. 3. Typical droplet size distribution, by volume, of emulsified cutting oil. Measured with Malvern MasterSizer S. Note sizes shown as diameter.

a 5 wt% emulsion was 1.1×10^{-3} kg/m/s. The oil droplet properties were measured by Malvern Instruments with a Malvern Zetasizer 3 (zeta potential and droplet size distribution by multi angle photo correlation spectroscopy) and a Mastersizer S (droplet size by low angle laser light scattering). The droplet diameter distribution was bimodal with two overlapping peaks at 100–1000 nm and 1–6 μm, Fig. 3. The size range and distribution characteristics of the oil droplets was also measured in our laboratory using a Granulometer HR 850 (Cilas-Alcatel) with similar characteristics. These droplet sizes are somewhat larger than those reported by Lipp et al. [20], who observed two peaks with overlapping distributions and a minimum-maximum range of 35–300 nm.

Two membranes were evaluated, the first was produced in our laboratories with Ultrason 6010 polyethersulfone (PES). The casting solution was prepared using 25 wt% PES, 5 wt% polyvinylpyrrolidinone (10,000 MW) and 70 wt% *N*-methylpyrrolidone. A 250 μm film was cast on a polyester backing (Hollitex, 3296) and then gelled in reverse osmosis water at 2°C. The characterization of this membrane with tap water flux and polyethylene glycol (PEG) retentions is summarized in Table 2 (permeability $l=1.05\times10^{-19}$ m^2 for Sherwood's correction factor). The effect of the

Table 2
Fluxes PEG solute retentions as a function of rotor speed, 310 kPa, 25°C, 200 ppm concentration

Membrane	Solute	Rotor speed (rpm)					
		0		100		1800	
		Flux (LMH)	Retention %	Flux (LMH)	Retention %	Flux (LMH)	Retention %
Ultrason 25–5	Tap water[bc]	101	na	97	na	77	na
	Tap water[ac]	145	na	140	na	109	na
	6 K PEG	109	2	120	39	108	100
	35 K PEG	44	39	77	85	96	102
	Tap water[ac]	117	na			93	na
HPES 50[ac]	Tap water			683[a]	na		

bc and *ac* indicate before and after cleaning with Ultrasil 10, 50°C and 0.5 wt%.
na – not available.
[a] Obtained at 900 rpm and 40 psi, corrected for backpressure.

rotor speed on the PEG retentions with the Ultrason membrane was considerable. The measured molecular weight cut off (MWCO) increased with higher rotor speeds and was attributable to decreasing the extent of concentration polarization and therefore higher observed retentions. A second membrane was purchased from Spintek Inc. and was described as a 50 kDa MWCO hydrophilic PES (henceforth designated as HPES 50). The permeability of this membrane (l=6.12×10^{-19} m^2) was determined from the flux pressure corrected curve at 900 rpm.

4. Experimental

Flux data with the Ultrason membrane were obtained using the full permeation area available. As will be seen in the following sections, the flux with this membrane was not mass transfer limited over a large range of operating conditions. The HPES 50 membrane was chosen because of its significantly higher initial pure water flux while still retaining >96% of the oil. A series of experiments using a restricted permeation area were performed with the HPES 50. Polycarbonate films were installed on the disc, covering the inner 80% of the membrane surface area.

Membranes were cleaned with 0.5 wt% Ultrasil 10 (Ecolab, MN, USA) for 20 min at 50°C to obtain the initial pure water flux, J_0. The flux and retentions were evaluated at approximately 5, 10 and 20 wt% cutting oil and various transmembrane pressures and rotor speeds. The higher concentrations (Ultrason 6010–25–5 only) were reached by diverting permeate from the recirculation tank to a separate container. Permeation experiments with the HPES 50 membrane were conducted at 5 wt% oil only.

At a given concentration, the transmembrane pressure and rotor speed were varied randomly and several replicates were performed under selected conditions. A final check on any flux hysteresis was performed by returning the collected permeate to the feed tank. The first stabilization period was approximately 50 min after the first exposure of the membrane to the cutting oil. Subsequently, a typical stabilization time for the flux was less than 10 min except at the lowest rotor speeds which was ~60 min. Fluxes were determined gravimetrically and the permeate returned to the feed tank. Permeate samples of 20 ml were taken for Total Carbon (TC) analysis (Shimadzu 5000 TOC). TC concentrations in the permeate stabilized at the same rate as fluxes.

5. Results and discussion

5.1. Ultrason 6010-25-5

5.1.1. Film theory

The permeate flux with the Ultrason 6010-25-5 membrane and 5 wt% cutting oil is shown in Fig. 4. Fluxes are linearly dependent on pressure at any rotor speed above 800 rpm. At rotor speeds above 1200 rpm, the permeate back pressure reduces the flux, for example, at 1800 rpm. When the flux is plotted as a function of the effective transmembrane pressure (Eq. (23)) the flux-pressure curves are co-linear for the rotor speeds 800–1800 rpm (not shown for clarity). This is essentially the same as the pure water flux observed after the initial membrane characterization (Table 2). The onset of mass transfer limited flux is seen at 275 kPa and 600 rpm, with the limiting flux being reached at 100 and 200 rpm.

Fig. 5 shows the flux obtained with a 5 wt% oil–water emulsion as a function of the rotor speed. The flux shows the expected increase at higher rotor speeds

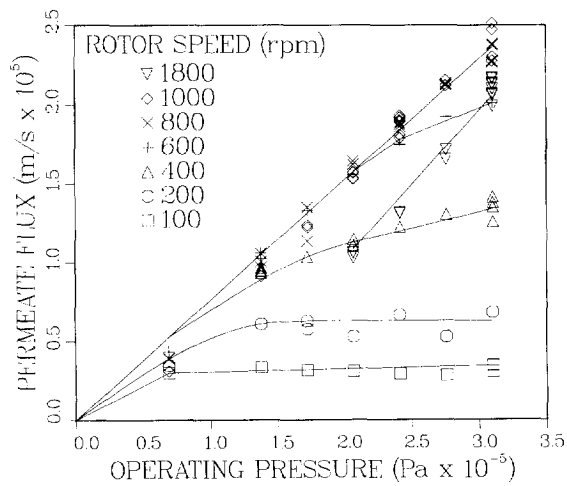

Fig. 4. Fluxes with Ultrason 6010-25-5 membrane as a function of pressure at various rotor speeds. 5 wt% cutting oil in water at 25°C. Lines are for clarity only.

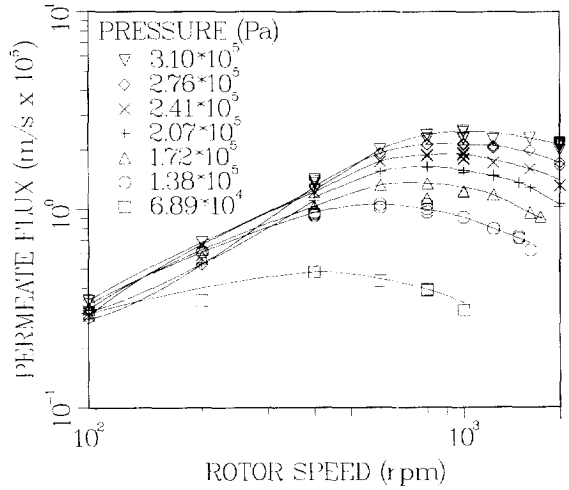

Fig. 5. Fluxes with Ultrason 6010-25-5 membrane as a function of rotor speed at various pressures. 5 wt% cutting oil in water at 25°C. Lines are for clarity only.

but then drops considerably after reaching a maximum. The initial flux increase was the result of reduced concentration polarization. As the rotor speed is increased, the pressure limited flux is reached. Further increases in the rotor speed resulted in lower fluxes as the increasingly significant permeate back pressure reduced the average transmembrane pressure. The rotor speed at which the maximum occurs is dependent on the operating pressure. At 69 kPa the maximum occurs at 400 rpm whereas at 310 kPa the maximum is observed at 1000–1200 rpm. Higher rotor speeds were required to offset the increasing transport of oil droplets to the membrane surface at the higher pressures. The declining flux at higher rpm observed in Fig. 5 is replaced by a plateau (figure not shown) when the pressure corrected flux, J_{vc}, is used.

The slope of the linear portion of these curves gives the exponent α in Eq. (4). The exponent was determined for each pressure and concentration, using only data in the mass transfer limited regime. The data in the plateau region was omitted in this analysis. The values of the exponents and the correlation co-efficient are listed in Table 3. Confidence intervals are not shown because they would be unduly large as the exponents at lower pressures are determined from only 2 or 3 data points.

Values for the exponent range from 0.6 to 1.12. Values for α greater than 1 may be the result of back transport by mechanisms other than Brownian diffusion, or simply experimental error. Quemeneur and Schlumpf [32] reported comparable values of 0.58 and 1.12 for laminar and turbulent flow, respectively with cutting oils in a small plate and frame cell. Goldsmith et al. [33] reported values between 1.1 and 1.15 for a 2.5 cm tubular system. Lipp et al. [20] obtained values of α between 0.48 and 0.64 which were in good agreement with the expected value of 0.57 for their flux model for stirred cell UF.

Table 3
Values for the exponent α of rotor speed in the film theory flux model, shown for various bulk concentrations and pressures. α determined from linear least squares of Fig. 4, ignoring the pressure limited flux region

Concentration oil emulsion wt %	Corrected pressure kPa (psi)	α	r
5	69 (10)	0.38	0.35
	138 (20)	0.76	0.99
	172 (25)	0.83	0.99
	207 (30)	0.89	0.99
	241 (35)	0.92	0.99
	276 (40)	0.99	0.98
	310 (45)	0.85	0.96
10	103 (15)	0.03	0.02
	172 (25)	0.64	na
	241 (35)	1.09	0.99
	310 (45)	0.66	0.91
20	103 (15)	0.36	0.62
	172 (25)	0.91	0.98
	241 (35)	1.12	0.99
	310 (45)	1.00	0.99

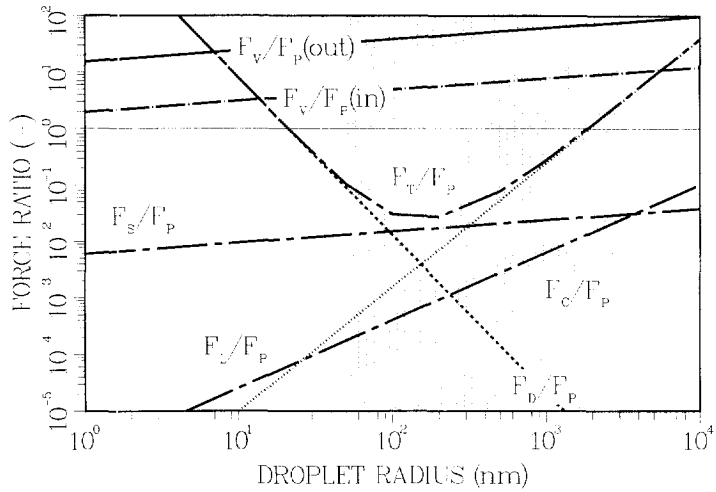

Fig. 6. Back transport mechanisms shown as a ratio of the equivalent force to the permeation drag force as a function of droplet radius. Note that F_T is the sum of F_S, F_B, F_{buoy} and F_L only, not F_V. Shaded area designates size range of oil droplets. Ultrason 6010-25-5 membrane, ΔP=310 kPa, ω=1800 rpm, 5 wt% cuttir g oil in water at 25°C.

Fig. 4 indicates that at sufficiently high rotor speeds there is minimal concentration polarization. Under conditions of concentration polarization the flux dependence on rotor speed can be adequately described by the film theory, although the flux dependence on the rotor speed is somewhat higher than expected. In the operating regime where the flux is pressure dependent, more insight can be gained by examining the forces exerted on a single droplet on the membrane surface.

5.1.2. Force balance on an oil droplet

The back transport forces are compared to the corrected permeation drag force of Sherwood and shown in Fig. 6. The test conditions were 800 rpm, 310 kPa and a flux of 85 LMH with 5 wt% oil. At this rotor speed, the flux is not mass transfer limited. The minimum in back transport observed by others for the combined back transport by lateral migration, Brownian and shear enhanced diffusion is still present. The dependence of the various back transport mechanisms on the droplet radius are also different from that customarily seen and is the result of using Sherwood's correction factor, Eq. (6). The correction factor is proportional to $r_p^{0.8}$ and ranges from 21 to 536 with droplet radii of 50 and 3000 nm, respectively.

The ratio of viscous/permeation drag forces, F_V/F_P, is considered separately as it is significant over a large range of droplet sizes and is a weak function of the droplet radius. Two lines are shown for F_V/F_P illustrating the difference of approximately one order of magnitude of the shear rate at the inner and outer radius of the disc, assuming a constant flux over the radius of the disc. The back transport ratios for the other mechanisms at the inner radius are not shown for clarity.

The remaining back transport mechanisms are highly dependent on the droplet radius and are comparable to the permeation drag at the upper and lower limit of the droplet size range. They are added and considered as the ratio F_T/F_P. F_T/F_P is much lower than unity for the majority of the droplet size range. At a droplet radius of 50 nm, F_T/F_P is primarily Brownian diffusion with F_B/F_P=0.11 and drops to a minimum of 0.03 at 100 nm where shear enhanced diffusion, F_S/F_P, dominates. Lateral migration is significant for a droplet radius of 3000 nm with F_L/F_P=2.8, but drops to less than unity for droplet radii smaller than ~2000 nm. Given that the flux shows no mass transfer limitations at this rotor speed, Fig. 4, back transport by viscous drag, even with the conservative estimate at the inner radius, appears to be indicated as the dominant back transport mechanism.

Back transport mechanisms of the oil droplets are also compared at different rotor speeds, in particular, at speeds where the flux begins to be mass transfer

Table 4
Ultrason 6010 membrane. Comparison of viscous drag force (F_V) and the summation of lateral migration, buoyancy, Brownian and shear enhanced diffusion forces (F_T), to the permeation drag force. Upper lower limits correspond to ratios at 50 and 3000 nm respectively

Rotor speed (rpm)	Flux (LMH)	F_V/F_P inner	F_T/F_P	Flux behaviour
100	10	6.8–15.3	0.8–0.1	Limiting flux
200	20	11.6–26.7	0.4–0.1	Limiting flux
400	49	16.7–38.0	0.2–0.4	Almost limiting flux
600	75	22.7–51.5	0.1–1.2	Onset of limiting flux
800	86	33.6–76.2	0.1–2.8	Linear flux-pressure

limited. Table 4 summarizes the back transport ratios F_V/F_P and F_T/F_P for different rotor speeds at the observed limiting flux. The range of ratios applies to the lower and upper limit of droplet sizes, respectively. This analysis is restricted to the 5 wt% oil data where the contribution of DLVO forces is negligible, Section 5.2.

F_V/F_P is greater than unity for the different limiting fluxes observed at each rotor speed. F_V/F_P is closest to unity at the lower rotor speeds and somewhat higher at rotor speeds greater than 400–600 rpm. However at these rotor speeds, the limiting flux is slightly higher and could not be reached because of the 310 kPa pressure limitation.

The ratio F_T/F_P approaches unity only at the extreme upper and lower limits of the droplet size. F_T/F_P is much smaller than unity for the bulk of the oil. Back transport by these mechanisms can be considered significant only if droplets at the upper and lower limits of the size range control the overall accumulation of droplets. Lipp et al. [20] found that using the smallest droplet size in their work with emulsified oils gave the best agreement with the film model. If this approach is used, Brownian diffusion predicts droplet accumulation with F_B/F_P=0.8 to 0.1, although this may be considered significant given the error involved in determining the various forces. At the upper limit of droplet sizes, the presence of larger droplets with a radius of 3000 nm could result in a scouring effect, disturbing the accumulated smaller droplets.

Centrifugal forces were not significant for any droplet size and would not be for any realistic density, being more than one order of magnitude below any other back transport mechanism. However, as suggested earlier, centrifugal effects could be significant in removing a gel layer which could have formed at lower rotor speeds.

5.2. Consideration of DLVO forces

DLVO forces were not considered in the previous discussions as their effect on droplet behaviour is more complex. DLVO forces can be very large compared to the forces described in the previous sections but their influence is significant over a very small distance. An important consideration is to first determine the Debye length for this system. A minimum value of M is based on the conductance of the tap water (125 μS (Ω^{-1})) used to prepare the oil mixtures. There are no added electrolytes in the cutting oil preparations other than the surfactants and emulsifiers. The Debye length based on the equivalent KCl concentration is ~10 nm. The conductivity of a 5 wt% oil–water emulsion was 550 S corresponding to a Debye length of ~4.8 nm. This approach to determine λ_D is only approximate. The effect of divalent/asymmetric ions is expected to result in a shorter λ_D due to the greater shielding of divalent ions compared to monovalent ions.

Fig. 7 shows the overall potential (J) for the oil–water emulsions with Debye length of 4.8 nm and zeta potential of −30 mV. For monodispersed droplets, the repulsive force is a function of the droplet size but the equivalent flux is not. The potential energy is essentially zero at a separation distance of 22 nm. At 20 nm the repulsive force (V_T/h) is equivalent to a permeation rate of 5.11×10^{-5} m/s (184 LMH (l/m^2/h)) and increases rapidly to a flux of $>1.39\times10^{-4}$ m/s (500 LMH) at a particle–particle separation of 18 nm.

We would like to determine if the droplet concentration at the membrane surface is high enough for

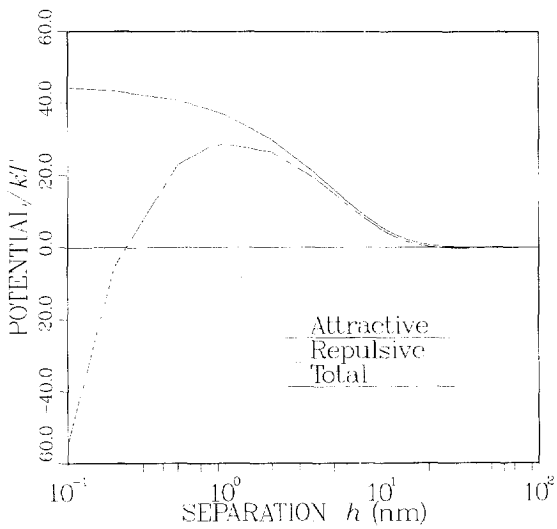

Fig. 7. Total interaction potential, V_T/kT, for two oil droplets as a function of separation distance. ζ=50 mV, r_p=50 nm and λ_D=4.8 nm.

electrostatic repulsion to be significant. Consider the case of two droplets with a radius of 50 nm which approach each other within 20 nm, as in the case of Fig. 7. We assume a maximum volume concentration of 0.646 for random dense packed monosized spheres. The volume fraction of oil in this situation, when we assume a droplet diameter of 50 nm±20 nm, would be ~0.24. For larger droplets, the volume fraction quickly approaches the limiting value of 0.646, as the 20 nm minimum approach distance becomes negligible compared to the droplet diameter. From the later discussions, it is clear that these concentrations are not reached at the membrane surface and that droplet separations are larger, and hence the repulsive forces negligible at these separation distances.

The sharp transition between weak attraction and strong repulsion essentially determines the minimum droplet–droplet and droplet–membrane separation distance. It's impact on membrane performance will be to influence the maximum packing or density of the concentration polarization layer. This is a significant factor in dense polarized layers or cakes [26].

The model of Bacchin et al. [28] warrants consideration as it, and back transport due to viscous drag, is significant in the size range where Brownian diffusion, shear enhanced diffusion and lateral migration are virtually nil. Using Eq. (12) is hampered by the lack of accurate estimates of the boundary layer thickness. Schlichting's [34] solution for the boundary layer thickness for a spinning disc in free space in turbulent flow,

$$\delta = 0.526r\left(\frac{\nu}{r^2\omega}\right)^{0.2} \tag{25}$$

gives $\delta \approx 2800$ μm at 1800 rpm. Calculated values for the potential energy barrier, V_B, range from 3.25×10^2 at 50 nm and increase rapidly to infinity with droplet size (10^{220} at 1000 nm). The critical fluxes calculated from Eq. (12) using these estimates of δ are less than 1 LMH. This boundary layer thickness is unduly large and accounts for the low fluxes. Hurwitz [30] obtained estimates of δ on the order of several microns, assuming an inertial sublayer existed between the viscous sublayer at the surface and the turbulent core. The critical flux for droplets between 50 and 1000 nm ranges from 8.6×10^{-5} to 11.1×10^{-5} m/s (310 to 400 LMH) for an assumed boundary layer thickness of 1 μm and drops by slightly more than one order of magnitude for a boundary layer thickness of 10 μm. Clearly it is difficult to make any conclusions regarding Bacchin et al.'s model (or any modified film model) without an accurate measure of δ.

5.3. Restricted permeation area, HPES 50 membrane

Difficulties in predicting the flux behaviour with the Ultrason membrane may have been due to averaging the flux and shear rates at different radii of the membrane disc. This problem was minimized by restricting the permeation area using an impermeable polycarbonate film which covered the inner 80% of the disc.

A different membrane (HPES 50) with a higher J_0 was used in this case. This allowed studying a higher range of permeation drag forces and determining the highest performance possible from this module configuration. Trends in performance were similar to those obtained with the Ultrason membrane, but with much higher fluxes. The maximum flux observed was 1.03×10^{-4} m/s (370 LMH) with the HPES 50 com-

Table 5
Comparison of fluxes with cutting oil emulsions with this work literature values

Reference	Pressure (bar)	Flux (LMH/bar)	Hydrodynamics (configuration & Re)	Oil conc. (wt%)
Goldsmith [33]	3.5	7–49	2.54 cm tubes, 64,000–150,000	1.7
Lee [37]	3.5	40–57	P & F, 860–2580	5
Quemeneur [32]	2	7–43	P & F, 400–7000	4.7
Lipp [20]	1	40	Stirred cell	5
Belkacem [36]	1	115[a]	P & F, 1.5 m/s	4
This work[a]	3	91	Spinning disc, 900,000	5
This work[b]	2.7	133	Spinning disc, 680,000	5

[a] No CaCl added to feed.
[b] Flux obtained for the full permeation area of the disc.
[c] Flux for the outer 20% of the membrane disc only.

pared to 2.58×10^{-5} m/s (93 LMH) with the Ultrason 6010. Deviations from pressure limited flux at 310 kPa were at 900 and 600 rpm for the HPES 50 and Ultrason 6010, respectively. TC concentrations were higher with the HPES 50 but the observed separation was still greater than 96%. Presumably still higher fluxes could be obtained with higher pressures. Higher fluxes could not be achieved by using a membrane with a higher J_0 (or MWCO) as the separation decreased to less than 80%.

Table 5 compares the fluxes obtained in this work with some from the literature in various configurations. This system had one of the highest pressure scaled fluxes at 91 LMH/bar (2.53×10^{-5} m/s/bar) for the full permeation area with a significantly higher flux at the outer perimeter. The important feature is that the other systems were operating under mass transfer limited conditions while the spinning disc system could benefit from higher operating pressures.

Using a restricted permeation area provided further indications that viscous drag is the dominant back-transport mechanism although the conclusions are not definite. Table 6 summarizes F_V/F_P and F_T/F_P at the various limiting fluxes and rotor speeds and are similar to the values obtained in the previous section. The limiting flux is underpredicted by F_V throughout a wide range of rotor speeds. A F_V/F_P ratio of 4.7–10.7 at a rotor speed of 100 rpm would predict a flux of $\sim4.2\times10^{-5}$ m/s (150 LMH), considerably higher than the observed flux of 8.1×10^{-6} m/s (29 LMH).

As in the previous section, back transport by Brownian diffusion or lateral migration are significant ($F_T/F_P>0.1$) at the extreme limits of the droplet size distribution. F_T/F_P is less than 0.1 for the majority of the droplet size distribution between 100 and 1000 nm radii. In general, values for both F_V/F_P and F_T/F_P are lower for the restricted permeation area experiments compared to the overall permeation results from Table 4. This brings F_V/F_P closer to unity while F_T/F_P for the remaining mechanisms becomes less significant.

Table 6
HPES 50 membrane. Comparison of viscous drag force (F_V) and the summation of lateral migration, buoyancy, Brownian and shear enhanced diffusion forces (F_T), to the permeation drag force. Note that permeation is through the outer 20% area of the membrane disc only

Rotor speed (rpm)	Flux (LMH)	F_V/F_P	F_T/F_P	Flux behaviour
100	29	4.7–10.7	0.54–0.04	Limiting flux
200	50	9.5–21.6	0.32–0.09	Limiting flux
400	100	16.6–37.7	0.16–0.43	Limiting flux
600	200	17.2–39.1	0.09–0.87	Limiting flux
900	370	19.3–43.8	0.05–2.0	Onset of limiting flux

Another important aspect of the restricted permeation experiment deals with the issue of DLVO forces. The maximum critical flux based on Bacchin et al.'s model was 11.1×10^{-5} m/s, with the lowest estimate of the boundary layer thickness of 1 μm. At 900 rpm the flux is just beginning to exhibit limiting behaviour and is almost at this critical value. At higher rpm and operating pressures, the critical flux would be easily exceeded, suggesting that DLVO forces do not dominate back transport.

Problems in predicting the onset of the limiting flux can arise from several factors, including: (1) estimates of the shear rate, (2) using a criteria for a backtransport to permeation drag ratio of at least unity for deposition, (3) Sherwood's correction factor for Stokes's law and (4) uncertainties about the true velocity of the permeate near a pore.

The assumption of an instantaneous response of an oil droplet to any force would result in overestimating the flux. Any delay in droplet removal after transport to the membrane surface would result in an accumulation of droplets to some degree. This would support viscous drag as the dominant mechanism as a force ratio greater than unity would be required.

Sherwood's correction factor is subject to considerable variation depending on the estimate of the skin layer thickness. A value of 1000 nm was used in Eq. (6) to determine the values in Tables 4 and 6. Reducing this estimate to 100 nm increases the correction factor by 2.5 and the force ratios are reduced by the same factor. This further supports viscous drag as the dominant back mechanism as F_V/F_P remains greater than unity and the remaining back transport ratios become less significant.

The permeation drag force on a droplet was evaluated using the measured flux. This does not account for the surface porosity of the membrane surface, which would result in a higher local velocity in the vicinity of a pore [19,20,35]. The importance of this correction depends on relative size of the droplet and pore and the pore to pore distance. Consider the case of an 8 nm radius pore, which corresponds to an ~50,000 MWCO, with a surface porosity of 10%. This corresponds to a pore center spacing of 45 nm assuming a cartesian grid. A droplet with a radius of 3000 nm would cover enough pores that the surface porosity correction for the local velocity would not be needed. Given a droplet size of 20 nm, then the need for a velocity correction is clear. For the present work the smallest oil droplet diameter of 100 nm would cover approximately four pores and a minor correction could be argued, but it would most likely be much smaller than $1/\varepsilon$. Any such velocity correction would increase the permeation drag, reducing both F_V/F_P and F_T/F_P bringing the former closer to the expected value of unity.

One may consider correcting the flux for the membrane surface porosity and using Sherwood's correction factor to account for the same phenomenon. This should not be the case as Sherwood's correction factor describes the balance between lubrification flow around the droplet and Darcy flow in the porous medium or membrane. The problem was described by Sherwood as equating (a) the force required to pull a sphere away from a porous medium with a given velocity to (b) the force on a sphere held at the membrane surface with flux of the same velocity.

6. Conclusions

Emulsified cutting oils were ultrafiltered with a commercial rotating membrane disc module. This module can operate at extremely high shear rates ($>10^5$ s^{-1}) which can be set independent of the bulk recirculation rate. Under mass transfer limited conditions, the flux behaviour was consistent with the film model with the flux proportional to $\omega^{0.75-1.2}$ over a wide range of operating pressures and bulk concentrations of 5, 10 and 20 wt% oil.

The onset of mass transfer limited flux was studied by evaluating forces acting on an oil droplet at the membrane surface. Improved resolution of the local flux and hydrodynamic conditions was obtained by restricting permeation to the outer portion of the membrane disc. Various back transport mechanisms, including lateral migration, Brownian and shear enhanced diffusion, were expressed as forces acting on the oil droplets. These were compared to the permeation drag force accounting for Sherwood's correction to Stokes's law for flow around a sphere over a permeable surface. Each back transport mechanism was expressed as a ratio of the permeation drag force. Ratios near to, or greater than, unity

suggested that back transport by that mechanism was possible.

Ratios of the viscous drag to permeation drag, F_V/F_P, ranged from 4.7 to 43.8 over a large range of operating conditions and all oil droplet sizes. Brownian diffusion was only significant (F_B/F_P=0.54–0.16) at the smallest droplet sizes and rotor speeds below 400 rpm. At 400 rpm and higher speeds, lateral migration became the alternate dominant back transport mechanism with F_L/F_P ranging from 0.43 to 2.00. However, these mechanisms were only significant at the extreme limits of the droplet size distribution, representing a small fraction of the droplet sizes. Over the majority of the droplet sizes, the observed flux was higher than expected based on the sum of lateral migration, Brownian and shear enhanced diffusion. DLVO forces play an important role by stabilizing the emulsions, however predictions of the limiting flux based on these forces underestimated the observed flux. Identifying the back transport mechanism controlling oil droplet behaviour at the membrane surface was primarily confounded by the large droplet size range (50–3000 nm).

7. List of symbols

A	area (m^2)
A	Hamaker constant (1×10^{-20} J)
D	diffusivity (m^2/s)
F_B	equivalent force due to Brownian motion (N)
F_C	centrifugal force (N)
F_L	equivalent force due lateral migration (N)
F_P	permeation drag force (N)
F_S	equivalent force due to shear enhanced diffusion (N)
F_T	total back transport force, not including viscous drag (N)
F_V	equivalent force due to viscous drag (N)
h	particle-particle or particle-surface separation distance (m)
J_0	measured flux with pure water (m/s)
J_v	measured flux with emulsified oil feed (m/s)
J_{vc}	flux corrected for permeate back pressure (m/s)
k	mass transfer coefficient (m/s)
k_B	Boltzman constant (1.4×10^{-23} J/K)
K	constant in Eqs. (19) and (21) (0.9)
l	membrane permeability (m^2)
M	molar concentration (mole/l)
P_{eff}	transmembrane pressure corrected for P_{perm} (kPa)
P_0	operating pressure (kPa)
P_{perm}	permeate backpressure (kPa)
r	radius of membrane disc (0.0921 m)
r_p	droplet or particle radius (m)
Re	Reynolds number, Re = $[d_h u_0 \rho/\mu](-)$
R_m	membrane resistance (m^{-1})
s	gap between membrane disc and wall (0.00635 m)
Sc	Schmidt number, Sc = $[\mu/\rho D](-)$
Sh	Sherwood number, Sh = $[kd_h/D](-)$
V_i	potential energy (J)

7.1. Greek Symbol

β	l/r_p^2 (–)
δ	boundary layer thickness (m)
δ_m	effective skin layer thickness of membrane (1×10^{-6} m)
ϵ	emissivity of water ($C^2/V/m$)
μ	dynamic viscosity (1.1×10^{-3} kg/m/s)
λ_D	Debye length (m)
ν	kinematic viscosity (m^2/s)
ω	angular velocity (rad/s)
ϕ	volume fraction of oil droplets (0.059)
ρ_l	density water (1000 kg/m)
ρ_p	density oil–oil droplet (850 kg/m)
τ	shear rate (s^{-1})
υ	velocity (m/s)
υ_B	characteristic droplet velocity due to Brownian diffusion (m/s)
υ_S	characteristic droplet velocity due to shear enhanced diffusion (m/s)
ε	membrane surface porosity (–)
ζ	zeta potential (mV)

Acknowledgements

The authors would like to thank Lysanne Bolduc for performing initial characterization and setup testing with the ST-IIL, Ken Darcovich (N.R.C.C.), Mark

Hurwitz (Pall Corporation) and Mark Wiesner (Rice University) for helpful discussions.

References

[1] G. Belfort, R.H. Davis, A.L. Zydney, The behavior of suspensions and macromolecular solutions in crossflow microfiltration, J. Membr. Sci. 96 (1994) 1–58.

[2] G. Belfort, J. Pimbley, A. Greiner, K.Y. Chung, Diagnosis of membrane fouling using a rotating annular filter. 1. Cell culture media, J. Membr. Sci. 77 (1993) 1–22.

[3] G. Belfort, P. Mikulasek, J. Pimbley, K.Y. Chung, Diagnosis of membrane fouling using a rotating annular filter. 2. Dilute suspensions of known particle size, J. Membr. Sci. 77 (1993) 23–39.

[4] A.-S. Jönsson, Influence of shear rate on the flux during ultrafiltration of colloidal substances, J. Membr. Sci. 79 (1993) 93–99.

[5] J.D. Sherwood, The force on a sphere pulled away from a permeable half-space, Physico Chemical Hydrodynamics 10(1) (1988) 3–12.

[6] M.E. O'Neill, A sphere in contact with a plane while in a slow linear shear flow, Chem. Eng. Sci. 23 (1968) 1293–1298.

[7] A.S. Michaels, New separation technique for the CPI, Chem. Engng. Prog. 64(12) (1968) 31–43.

[8] J. Murkes, C.G. Carlsson, Crossflow Filtration: Theory and Practise, Wiley, 1988.

[9] M.C. Porter, Concentration polarization with membrane ultrafiltration, Ind. Chem. Prod. Res. Develop. 11(3) (1972) 234–248.

[10] W.F. Blatt, A. Dravid, A.S. Michaels, L. Nelsen, in: J.E. Flinn (Ed.), Membrane Science and Technology, Plenum press, New York, 1970.

[11] A.G. Fane, Ultrafiltration of suspensions, J. Membr. Sci. 20 (1984) 249–259.

[12] V. Lahoussine-Turcaud, M.R. Wiesner, J.-Y. Bottero, Fouling in tangential-flow ultrafiltration: the effect of colloid size and coagulation pretreatment, J. Membr. Sci. 52 (1990) 173–190.

[13] M.R. Wiesner, M.M. Clark, J. Mallevialle, Membrane filtration of coagulated suspensions, J. Environmental Eng. 115(1) (1989) 20–40.

[14] P. Schmitz, D. Houi, B. Wandelt, Hydrodynamic aspects of crossflow microfiltration. Analysis of particle deposition at the membrane surface, J. Membr. Sci. 71 (1992) 29–40.

[15] C. Rosén, C. Trägåth, Computer simulations of mass transfer in the concentration boundary layer over ultrafiltration membranes, J. Membr. Sci. 85 (1993) 139–156.

[16] M.-C. Aubert, M.-P. Eulluard, H. Barnier, Shear stress induced erosion of filtration cake studied by a flat rotating disk method. Determination of the critical shear stress of erosion, J. Membr. Sci. 84 (1993) 229–240.

[17] W.M. Lu, S.C. Ju, Selective particle deposition in crossflow filtration, Sep. Sci. Technol. 24(7)–8 (1989) 517–540.

[18] K. Stamatakis, C. Tien, A simple model of cross-flow filtration based on particle adhesion, AIChE J. 39(8) (1993) 1292–1302.

[19] A.G. Fane, C.J.D. Fell, A.G. Waters, The relationship between membrane surface pore characteristics and flux for ultrafiltration membranes, J. Membr. Sci. 9 (1981) 245–264.

[20] P. Lipp, C.H. Lee, A.G. Fane, C.J.D. Fell, A fundamental study of the ultrafiltration of oil-water emulsions, J. Membr. Sci. 36 (1988) 161–177.

[21] M.R. Wiesner, S. Chellam, Mass transport considerations for pressure-driven membrane processes, J. AWWA 84(1) (1992) 88–95.

[22] D.T. Leighton, A. Acrivos, Measurement of the shear induced coefficient of self-diffusion in concentrated suspensions of spheres, J. Fluid Mech. 177 (1987) 109–131.

[23] R.D. Cohen, R.F. Probstein, Colloidal fouling of reverse osmosis membranes, J. Coll. Interface Sci. 114(1) (1986) 194–207.

[24] D.A. Drew, J.A. Schonberg, G. Belfort, Lateral inertial migration of a small sphere in fast laminar flow through a membrane duct, Chem. Eng. Sci. 46(12) (1991) 3219–3224.

[25] R.F. Probstein, Physicochemical Hydrodynamics, An Introduction, Buttersworth, Boston, 1989.

[26] S.P. Palecek, A. Zydney, Hydraulic permeability of protein deposits formed during microfiltration: effect of solution pH and ionic strength, J. Membr. Sci. 95 (1994) 71–81.

[27] R.M. McDonogh, A. G Fane, C.J.D. Fell, Charge effects in the cross-flow filtration of colloids and particles, J. Membr. Sci. 43 (1989) 69–85.

[28] P. Bacchin, P. Aimar, V. Sanchez, Model for colloidal fouling of membranes, AIChE J. 41(2) (1995) 368–376.

[29] A.A. Kozinsky, E.N. Lightfoot, Protein ultrafiltration: A general example of boundary layer filtration, AIChE J. 18(5) (1972) 1030–1040.

[30] M. Hurwitz, J. Brantley, Scaling of rotating disc dynamic filter processes, 8th Annual Meeting of the North American Membrane Society, Ottawa, Canada, May, 1996.

[31] M.R. Wiesner, J. Engler, Development of a rotating disk membrane for treating aqueous streams with high solids concentrations, 8th Annual Meeting of the North American Membrane Society, Ottawa, Canada, May, 1996.

[32] F. Quemeneur, J.P. Schlumpf, Traitement des huiles solubles par ultrafiltration, Entropie 93 (1980) 22–29.

[33] R.L. Goldsmith, D.A. Roberts, D.L. Burre, Ultrafiltration of soluble oil wastes, Journal WPCF 46(9) (1974) 2183–2192.

[34] H. Schlichting, Boundary-Layer Theory, McGraw Hill Book Company, New York, 6th ed., 1968.

[35] J.L. Gaddis, S. Datta, Polarization adjacent to an inhomogeneous membrane, Sep. Sci. Technol. 25(13)–15 (1990) 1421–1439.
[36] M. Belkacem, M. Matamoros, C. Cabassud, Y. Aurelle, J. Cotteret, New results in metal working wastewater treatment using membrane technology, J. Membr. Sci. 106 (1995) 195–205.
[37] S.B. Lee, Y. Aurelle, H. Roques, Etude de l'ultrafiltration d'une emulsion d'huile de coupe, Entropie 121 (1985) 30–44.